Research Square

Preprints are preliminary reports that have not undergone peer review.
They should not be considered conclusive, used to inform clinical practice,
or referenced by the media as validated information.

Correlations between Structural Disorder, Electronic States, and Charge Transport in AlCo, AlZn, FeCo, and FeZn Layered Double Hydroxide

Mennatullah A. Ghaleb
Cairo University
Rabab M. El-Sherif
Cairo University
Khaled Faisal Qasim
Suez University
M. M. El-Desoky
mmdesoky@suezuniv.edu.eg

Suez University

Research Article

Keywords: LDHs, SPH, VRH, TEP, XPS

Posted Date: November 20th, 2026

DOI: https://doi.org/10.21203/rs.3.rs-11462505/v1

License: This work is licensed under a Creative Commons Attribution 4.0 International License.
Read Full License

Additional Declarations: No competing interests reported.

Correlations between Structural Disorder, Electronic States, and Charge Transport in AlCo, AlZn, FeCo, and FeZn Layered Double Hydroxide

Mennatullah A. Ghaleb[1], Rabab M. El-Sherif[1], Khaled Faisal Qasim[2], M. M. El-Desoky*[3]

[1] Faculty of Postgraduate Studies for Nanotechnology, Cairo University, Giza, Egypt

[2]Chemistry Department, Faculty of Science, Suez University, 43518, Egypt

[3]Physics Department, Faculty of Science, Suez University, 43518, Egypt

Abstract

Layered double hydroxides (LDHs) are promising 2D materials, but their electrical transport mechanisms remain strongly dependent on composition. Here, four equimolar (1:1) LDHs (AlCo, AlZn, FeCo, and FeZn) were synthesized by PVA-assisted co-precipitation and investigated using XRD, TEM/SAED, XPS, electrical conductivity, and thermoelectric power measurements. The Al-based samples showed more ordered crystalline structures, whereas the Fe-based samples exhibited greater structural disorder. Temperature-dependent transport analysis revealed non-adiabatic small-polaron hopping (SPH) at higher temperatures and Greaves' variable-range hopping (VRH) behavior in the intermediate-temperature regime. The SPH assignment was supported by the Holstein–Emin bandwidth criterion, the calculated-to-experimental temperature comparison, and Meyer–Neldel compensation behavior. The apparent activation energy ranged from 0.397 eV for AlZn to 0.981 eV for FeZn. At 400 K, AlZn exhibited the highest reported conductivity and calculated hopping mobility (1.19×10^{-4} cm^2 V^{-1} s^{-1}), whereas FeZn showed the lowest mobility (9.70×10^{-8} cm^2 V^{-1} s^{-1}). These findings highlight the role of carrier mobility, alongside composition and local structure, in governing electrical transport in equimolar LDHs.

Keywords: LDHs; SPH; VRH; TEP; XPS

Corresponding author: E-mail: mmdesoky@suezuniv.edu.eg

1. Introduction

Two-dimensional (2D) layered double hydroxides (LDHs), commonly known as hydrotalcite-like anionic materials, have attracted considerable research interest in advanced functional materials, solid-state electronics, and energy applications owing to their positively charged brucite-like host layers, highly tunable chemical composition, and flexible interlayer spacing [1, 2]. The structural framework of LDHs is generally represented by the chemical formula $[M^{2+}_{1-x}M^{3+}_{x}(OH)_2]^{x+}[A^{n-}]_{x/n}.mH_2O$, where partial substitution of divalent

metal cations (M^{2+}: Co^{2+}, Zn^{2+}, Ni^{2+}, and Fe^{2+}) by trivalent metal cations (M^{3+}: Al^{3+} and Fe^{3+}) generates a net positive charge within the hydroxide layers. This positive charge is electrostatically compensated by intercalated solvated anions (A^{n-}: CO_3^{2-}, NO_3^- , and Cl^-) [3, 4]. The tunable crystal architecture and abundance of surface-active sites have made LDHs attractive candidates for surface-dominated processes, including pseudocapacitive charge storage and heterogeneous catalysis [5, 6]. However, the practical utilization and device integration of pristine LDHs remain significantly limited by their intrinsically low electrical conductivity ($\sigma < 10^{-6}$ S.m^{-1}), high intersheet contact resistance, and structural instability associated with layer restacking and particle agglomeration [7, 8].

To overcome these transport limitations, previous research has relied on external modification strategies, including the incorporation of conductive carbonaceous scaffolds such as graphene oxide and carbon nanotubes, as well as the construction of complex core-shell heterostructures [9, 10]. Moreover, most reported LDH systems have focused on non-equimolar compositions, typically employing M^{2+}:M^{3+} ratios of 2:1, 3:1, or 4:1, based on the assumption that equimolar metal ratios may result in less stable phases and poorer physical properties [4, 11]. However, these approaches largely overlook the intrinsic charge-transport processes occurring within the pristine LDH host lattice. In particular, the mechanisms controlling carrier transport through the metal-oxygen-metal (M-O-M) bonding network remain insufficiently understood. Rather than considering the low electrical conductivity of LDHs solely as a limitation that must be overcome through external conductive additives, investigating the basic mechanism of charge transport as a function of cation identity and coordination environment may provide a rational pathway toward atomic-scale transport engineering.

In semiconducting transition-metal compounds containing mixed-valence cations, electrical conduction can occur through phonon-assisted small polaron hopping (SPH) between localized electronic states rather than conventional free-electron band transport [12, 13]. Strong electron-phonon interactions can induce local lattice distortion and trap charge carriers within localized potential wells, resulting in the formation of small polarons [14, 15]. Charge transfer can then occur through thermally activated hopping between neighboring multivalent cation sites, such as Co^{2+}/Co^{3+} and Fe^{2+}/Fe^{3+}, through bridging oxygen pathways [16, 17]. According to the non-adiabatic small polaron hopping model, electrical conductivity is strongly influenced by the intersite separation (R), local dielectric environment, overlap of transition-metal electronic states, and fraction of available hopping sites (c) [13, 18]. In addition to these atomic-scale parameters, microstructural characteristics such as crystallite size (D) and lattice strain (ε) can substantially influence overall charge transport. Grain boundaries, and structural defects may introduce local potential barriers, increase carrier scattering, and consequently modify the overall electrical conductivity [19, 20].

Despite extensive investigations of small polaron conduction in transition-metal oxides, glasses, and multiferroic materials [13, 16], detailed studies addressing the intrinsic electrical transport, polaron hopping kinetics, and thermoelectric power (TEP) behavior of 2D layered double hydroxides remain limited. In particular, a comprehensive understanding of the small polaron hopping parameters, hopping carrier mobility (μ), and variable-range hopping (VRH) behavior in equimolar multicomponent LDH systems has not yet been established. Determining whether charge transport in 2D LDH frameworks proceeds through adiabatic or non-adiabatic hopping, and understanding how different cation combinations, including Al-Co, Al-Zn, Fe-Co, and Fe-Zn, influence localized electronic transitions, are therefore important for developing a clear understanding of charge transport in these two-dimensional inorganic lattices.

In this work, we systematically investigate the structural characteristics, surface oxidation states, and electrical transport mechanisms of four equimolar (1:1) LDH systems, namely AlCo, AlZn, FeCo, and FeZn LDHs, synthesized using a scalable and environmentally benign co-precipitation method. The crystal structure, nanoscale morphology, and local structural ordering are investigated using X-ray diffraction (XRD) and high-resolution transmission electron microscopy combined with selected-area electron diffraction (HRTEM/SAED). High-resolution X-ray photoelectron spectroscopy (XPS) is employed to resolve the different metal oxidation states (M^{2+}/M^{3+}) and quantitatively determines the corresponding hopping-site fractions (c) relevant to small polaron transport. Temperature-dependent direct-current electrical conductivity (σ) and thermoelectric power (TEP, Seebeck coefficient) measurements are performed to determine the dominant charge-carrier type, investigate the thermally activated transport mechanism, evaluate the polaron hopping activation barrier (W_H), and assess the applicability of Mott's small polaron hopping model together with Greaves' intermediate-temperature variable-range hopping (VRH) framework. This study provides a comprehensive correlation between metal oxidation states, crystallographic and microstructural characteristics, and macroscopic electrical transport, thereby establishing a fundamental framework for understanding charge conduction in equimolar 2D layered double hydroxides.

2. Experimental procedure

Four distinct layered double hydroxide (LDH) matrices, designated as Al–Co, Al–Zn, Fe–Co, and Fe–Zn LDHs, were fabricated through a controlled co-precipitation route as illustrated in **Fig.1**. High-purity high-purity reagents, including aluminum chloride hexahydrate ($AlCl_3 \cdot 6H_2O$), cobalt chloride hexahydrate ($CoCl_2 \cdot 6H_2O$), zinc chloride ($ZnCl_2$), ferric nitrate nonahydrate [$Fe(NO_3)_3 \cdot 9H_2O$], ammonium hydroxide (NH_4OH), and polyvinyl alcohol (PVA), were procured from Loba Chemie Pvt. Ltd. (India) and utilized without further purification. Deionized water was employed as the reaction medium throughout all processing stages. In a typical synthesis, calculated amounts of the trivalent (Al^{3+} or Fe^{3+}) and divalent (Co^{2+} or Zn^{2+})

precursors were dissolved in 100 mL of deionized water under vigorous magnetic stirring to maintain an equimolar cation ratio (M^{3+}:M^{2+} = 1:1). Concurrently, a separate aqueous solution containing 0.12 g of PVA in 50 mL of deionized water was introduced dropwise into the mixed metal salt solution to act as a polymer capping agent, thereby moderating nucleation kinetics and reducing particle agglomeration. The reaction medium was then adjusted to a constant pH of 8.0 through the dropwise addition of diluted ammonium hydroxide. The resulting suspensions were subsequently kept under gentle stirring at room temperature for 1 h to facilitate phase crystallization while limiting excessive crystal growth, thereby preserving the flexible 2D nanosheet morphology. The solid precipitates were separated by filtration, thoroughly washed several times with deionized water to eliminate residual spectator ions, and dried at 50 °C for 2 h under ambient atmosphere to produce the final LDH powders.

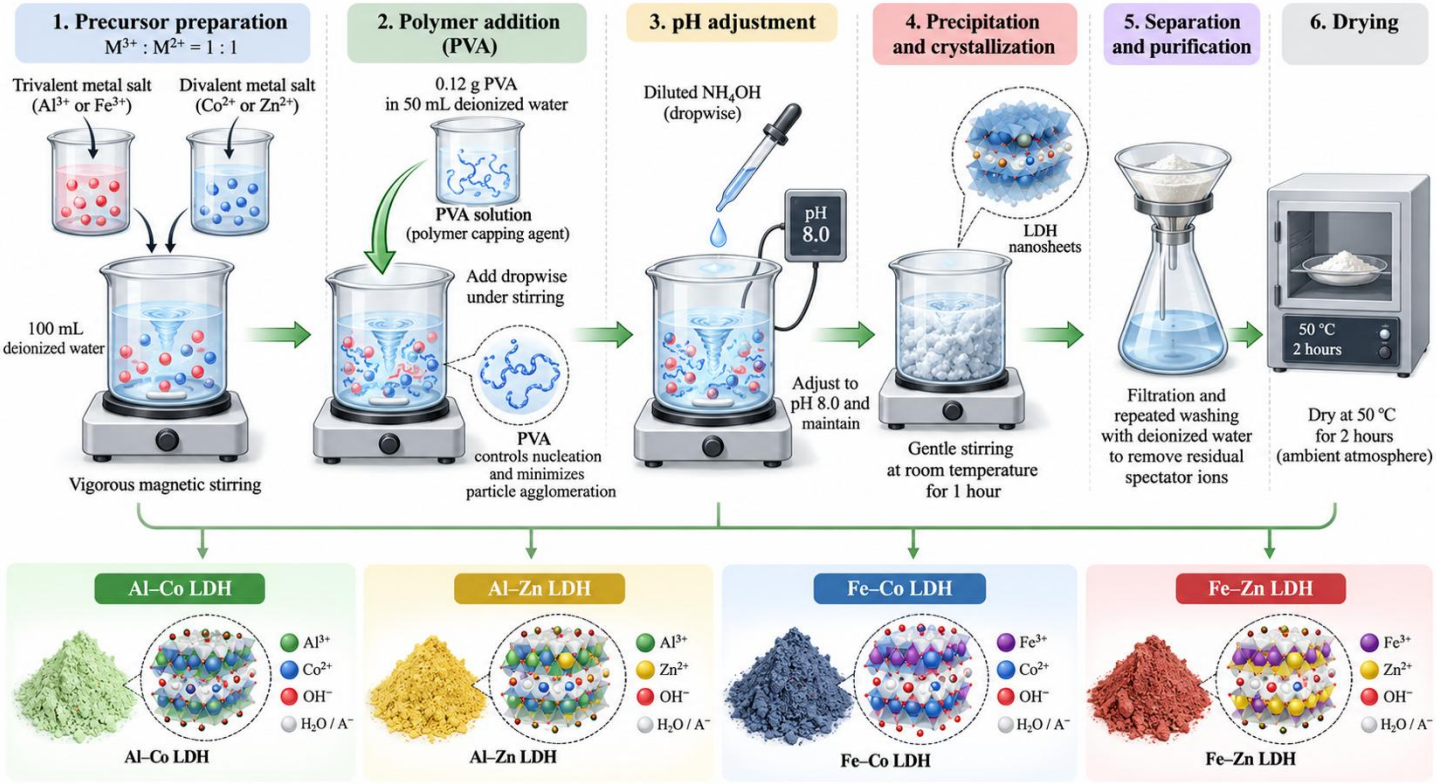

Fig. 1 Schematic diagram of experimental workflow

For structural and phase identification, powder X-ray diffraction (XRD) patterns were collected at ambient temperature using a Philips XL 40 diffractometer equipped with Cu Kalpha radiation (lambda = 0.154 nm), operated over a *2θ* scanning range of 10°–80°. The morphological features, particle size distributions, and selected area electron diffraction (SAED) patterns were obtained using a high-resolution transmission electron microscope (HRTEM, JEOL JEM-2100). The surface elemental composition, metal oxidation states, and

hopping site distributions were analyzed by X-ray photoelectron spectroscopy (XPS) on a KRATOS XSAM-800 spectrometer utilizing a monochromatic Al Kα radiation source, where all recorded binding energies were systematically charge-referenced to the adventitious C 1s peak at 284.8 eV. For macroscopic physical and transport characterizations, the synthesized LDH powders were uniaxially compressed into dense cylindrical pellets (13 mm diameter) using a hydraulic press. The bulk density (ρ) of the compressed pellets was determined at room temperature (298 K) in accordance with Archimedes' principle of liquid displacement, with measurements conducted in triplicate to guarantee statistical accuracy. For electrical transport measurements, both flat surfaces of the polished pellets were coated with a thin layer of conductive silver paste to serve as ohmic electrodes. The dc electrical conductivity (σ) was measured as a function of temperature over the range of 333–453 K using a KEITHLEY 485 autoranging picoammeter connected in series with a stable dc voltage supply. The thermoelectric power (TEP, Seebeck coefficient) measurements were performed in the temperature range of 310–470 K using two copper electrodes and two calibrated K-type digital thermocouples connected to the sample surfaces across a temperature difference maintained across the sample.

3. Results and discussion

3.1. X-ray diffraction analysis (XRD)

The room-temperature X-ray diffraction patterns of the synthesized samples are displayed in **Fig. 2. (a)**. The Al-containing materials (AlCo and AlZn) exhibit sharp, well-defined diffraction profiles characteristic of long-range periodic stacking, while the Fe-based counterparts (FeCo and FeZn) display broad, weak diffraction features over the 2θ range of approximately 20-40°, suggesting a disordered, nanocrystalline or quasi-amorphous network. For the crystalline AlCo and AlZn lattices, the diffraction reflections indicate the formation of a single-phase hydrotalcite-like layered double hydroxide (LDH) framework crystallized in the 3R rhombohedral polytype with space group R-$\bar{3}$m [1] .

For AlCo and AlZn, the low-angle reflection near 2θ ≈11-12° is assigned to the (003) plane, while the reflection around $2\theta \approx$22-23° corresponds to the (006) plane. Additional reflections at higher diffraction angles were examined to identify the non-basal crystallographic planes and evaluate the layered structure. The experimental patterns were compared with the standard JCPDS reference cards (00-038-0486) [2] . In contrast, the broad features observed for FeCo and FeZn suggest substantial structural disorder; therefore, definitive phase identification requires careful comparison with the appropriate reference patterns. This loss of long-range translational symmetry in FeCo and FeZn stems directly from the rapid hydrolysis kinetics and extremely low solubility product (K_{sp}) of Fe^{3+} species during chemical co-precipitation, which promotes local lattice distortions and structural disorder [3].

To quantify the structural dimensions, the pattern is indexed within a hexagonal unit cell setting (a = b ≠ c), where the in-plane parameter (a) and the axial stacking parameter (c) are deduced from the symmetric (110) and basal (003) reflections, respectively:

$$\boldsymbol{a = 2d_{110}} \quad \mathbf{(1)}$$

$$\boldsymbol{c = 3d_{003}} \quad \mathbf{(2)}$$

The corresponding unit cell volume (V) for the hexagonal framework was computed via:

$$\boldsymbol{V = \frac{\sqrt{3}}{2} a^2 c} \quad \mathbf{(3)}$$

As summarized in **Table 1**, the unit cell volume increases moderately from 181.0 Å^3 for AlCo to 184.7 Å^3 for AlZn, mainly caused by the expansion of the basal stacking axis (c = 22.3 Å to 22.8 Å). This expansion is directly translated into the molar volume ($V_m = V.N_A / Z$, where Z = 3 is the formula units per hexagonal unit cell), reflecting the addition of larger ionic species (Zn^{2+}, Shannon ionic radius r = 0.74 Å) relative to octahedral Co^{2+} (r = 0.65 Å low spin), accompanied by hydration variations within the intercalated layers [4] .Furthermore, the theoretical X-ray crystallographic density (ρ_{xrd}) was determined from the unit cell dimensions:

$$\boldsymbol{\rho = \frac{Z * M}{N_A * V_{cell}}} \quad \mathbf{(4)}$$

where M denotes the molar mass of the LDH formula unit and N_A is Avogadro's number. The theoretical densities align closely with the bulk density and electrical conductivity derived from Arrhenius conductivity analysis. To separate the combined effect of crystallite size and internal lattice strain, the Williamson-Hall (W-H) uniform deformation model was applied to the main diffraction peaks [5] :

$$\boldsymbol{\beta \cos\theta = \frac{K\lambda}{D} + 4\varepsilon \sin\theta} \quad \mathbf{(5)}$$

Where β is the full width at half maximum (FWHM) in radians, θ is the Bragg diffraction angle, K = 0.9 is the Scherrer shape factor, λ= 1.5406 Å is the Cu-Kα wavelength, D is the average crystallite size, and ε represents the lattice microstrain. As shown in the linear Williamson-Hall plots **Fig.2 (b)**, the crystallite size increases from 5.8 nm for AlCo to 7.7 nm for AlZn, while the microstrain concurrently decreases from 6.0×10^{-3} to 4.5×10^{-3}. This opposite trend demonstrates that grain growth reduces internal boundary limitations, thereby reducing residual lattice stresses and dislocation densities [5]. This internal stress relaxation in AlZn creates a

less strained local structure that explains its lower polaron hopping barrier (W_H), high sensitivity during thermal transport, and higher electrical conductivity, as shown in **Fig. 2(c)** as discussed in the following sections.

Sample ID	a (Å)	c (Å)	V_{cell} (Å^3)	$V_m \pm 0.02$ (cm^3.mol^{-1})	$\rho_{xrd} \pm 0.02$ (g·cm^{-3})	D ± 1 (nm)	ε (×10^{-3})
AlCo	3.07	22.3	181	36.33	2.95	5.8	6
AlZn	3.06	22.8	184.7	37.08	2.82	7.7	4.5

Table 1. Crystallographic parameters for the Al-based LDH samples derived from XRD analysis.

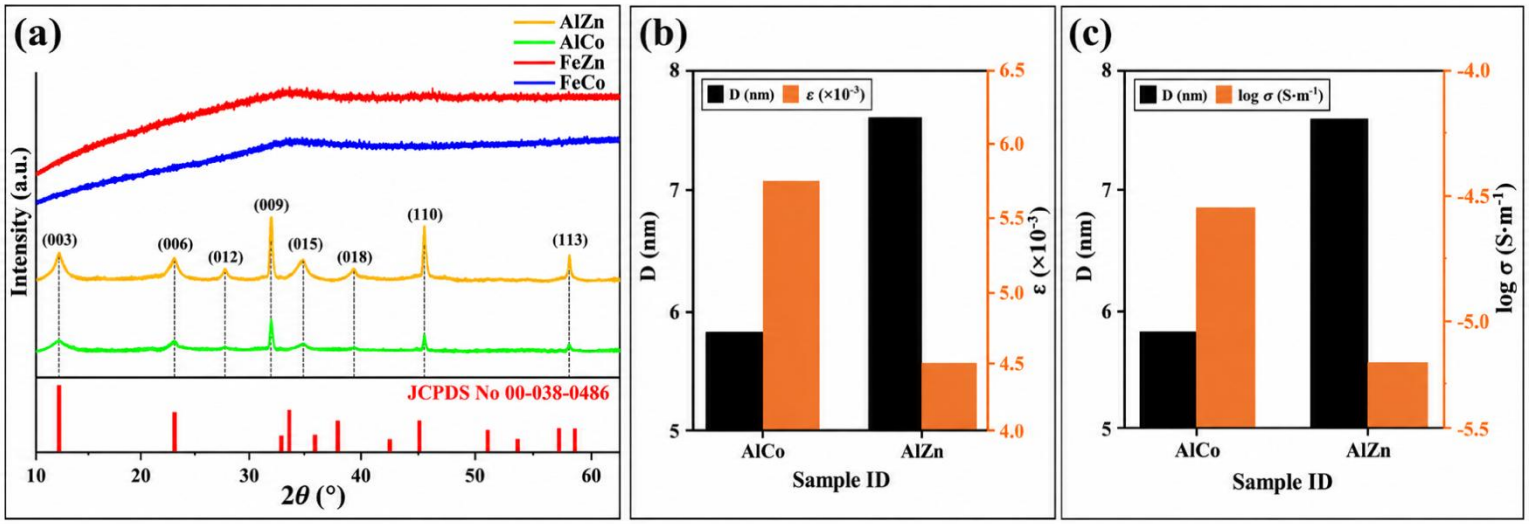

Fig. 2 XRD patterns and correlations between crystallite size, microstrain, and electrical conductivity of the LDH samples.

3.2. Microstructural Analysis (TEM and SAED)

The morphology, particle dimensions, and local structure of the prepared samples were investigated using transmission electron microscopy (TEM) and selected area electron diffraction (SAED), as shown in **Fig. 3**. The bright-field TEM images show clear differences in shape and size depending on the sample composition. For the Al-based, the images reveal typical layered nanosheets with distinct flexible boundaries (**Fig. 3a and 3b**). The sheets are slightly folded and crumpled at the edges, which is a common feature of two-dimensional layered double hydroxides. The measured particle sizes for these two samples range between 10 and 22 nm. In contrast, the Fe-based samples (**Fig. 3c and 3d**) displays smaller, densely packed nanoparticles with an average size of only 2.9 to 5.2 nm. This notable reduction in particle size occurs because Fe^{3+} ions precipitate and hydrolyze much faster than Al^{3+} ions during synthesis. This rapid precipitation leads to high nucleation rates with limited particle growth, forming very fine and disordered clusters [3] .The local crystalline structure was further evaluated using SAED. As presented in **Fig. 3a*** and **3b***, both AlCo and AlZn display clear concentric

diffraction rings with bright spots. This pattern confirms that these samples are polycrystalline with well-ordered layers matching the hydrotalcite rhombohedral structure (R-$\bar{3}$m). On the other hand, the SAED pattern of FeCo and FeZn (**Fig. 3c*, d***) shows only a diffuse, blurry halo without sharp rings or spots. This confirms that FeCo lacks long-range atomic order and has a quasi-amorphous or highly disordered nature.

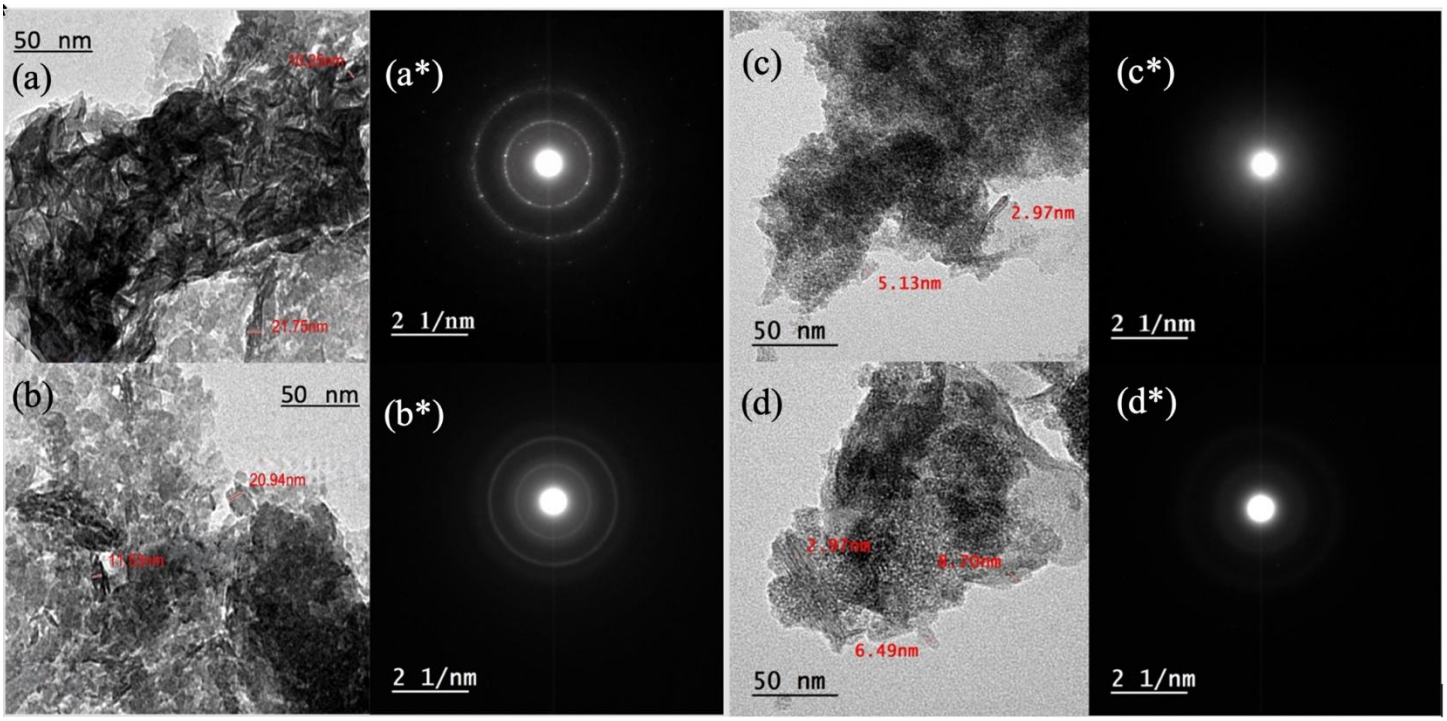

Fig. 3 TEM micrographs and SAED patterns of the synthesized samples: **(a, a*)** AlCo; **(b, b*)** AlZn; **(c, c*)** FeCo; **(d, d*)** FeZn

3.3. X-ray photoelectron spectroscopy (XPS) and hopping fraction analysis

High-resolution X-ray photoelectron spectroscopy (XPS) was conducted to investigate the chemical states, surface oxidation states, and to quantitatively determine the fraction of hopping transition metal sites (c) controlling small polaron transport. As shown in the survey spectra **Fig. 4(a)**, the characteristic core levels of the constituent elements (Al, Fe, Co, Zn, and O), together with adventitious C 1s, are observed. No detectable signals associated with residual chloride (Cl 2p at approximately 198 eV) or nitrate (N 1s at approximately 400 eV) species were observed, suggesting effective purification. Atmospheric carbonate species (CO_3^{2-}) may act as charge-balancing interlayer anions within the brucite-like galleries.

Within the non-adiabatic small polaron hopping (SPH) theory, charge transport in transition metal systems relies on phonon-assisted electron transfer between adjacent multivalent cation sites such as $Co^{2+} \leftrightarrow Co^{3+}$ and $Fe^{2+} \leftrightarrow Fe^{3+}$ [6]. The fraction of low-valence active sites (c) was evaluated from the integrated areas of

the deconvoluted 2p core-level peaks, taking into account both the $2p_{3/2}$ and $2p_{1/2}$ components along with their associated satellite peaks:

$$A_{M^{2+}} = A_{M^{2+},2p_{\frac{3}{2}}} + A_{M^{2+},2p_{\frac{1}{2}}} \quad (6)$$

$$A_{M^{3+}} = A_{M^{3+},2p_{\frac{3}{2}}} + A_{M^{3+},2p_{\frac{1}{2}}} \quad (7)$$

$$c = \frac{A_{M^{2+}}}{(A_{M^{2+}} + A_{M^{3+}})} \quad (8)$$

where $A_{M^{2+}}$ and $A_{M^{3+}}$ represent the total integrated peak areas corresponding to the divalent and trivalent oxidation states, respectively. Importantly, this hopping fraction (c) was not evaluated for the AlZn sample because its constituent cations Al^{3+} and Zn^{2+} exhibit stable oxidation states. Al^{3+} has the electronic configuration [Ne], whereas Zn^{2+} has a filled $3d^{10}$ subshell. Consequently, conventional intervalence hopping between Al^{3+} and Zn^{2+} is not expected [7] .

In contrast, AlCo, FeCo, and FeZn possess accessible mixed-valence states, allowing the extraction of c, as illustrated in **Fig. 4(b)**. In polaron conduction theory, the effective concentration of hopping pairs is proportional to c (1 - c), which reaches its maximum theoretical value when c = 0.50 (an equimolar 1:1 mixture of donor and acceptor states) [6], [8] . The calculated c values for the investigated samples are summarized in **Table 3**. AlCo exhibits a near-equimolar distribution of Co^{2+} and Co^{3+} ($c \sim 0.526$) optimizes the carrier transfer probability, thereby providing a fundamental explanation for the low polaron hopping activation barrier (W_H = 0.598 eV). In FeCo exhibits a higher ferrous (Fe^{2+}) content approximately 70.64%, whereas FeZn displays a more balanced distribution. Despite the c value in FeZn is (~ 0.469), this material suffers from severe electronic localization and displays the highest hopping activation energy (W_H = 0.981 eV) and lowest electrical conductivity. This behavior is discussed further in the electrical transport analysis.

To further investigate the local chemical environments, the high-resolution core-level spectra were deconvoluted, as shown in **Fig.4 (c)**. The O 1s spectra were fitted with components assigned to lattice oxygen (M–O) at 529.7–530.1 eV, oxygen-defect-related species at approximately 531.5 eV, structural hydroxyl groups (M–OH) at approximately 532.8 eV, and adsorbed or interlayer water at approximately 535.0 eV. The Al 2p signal occurs at 73.5–74.2 eV and is consistent with Al^{3+}. The Zn 2p spectrum exhibits peaks at 1021.8 eV (Zn $2p_{3/2}$) and 1044.8 eV (Zn $2p_{1/2}$), with a spin–orbit separation of approximately 23.0 eV, characteristic of Zn^{2+}. The Co 2p spectra contain contributions assigned to Co^{2+} at 782.6 and 798.1 eV and Co^{3+} at 780.4 and 796.2 eV, accompanied by shake-up satellite features at approximately 786.5 and 803.0 eV. Similarly, the Fe 2p

spectra show components assigned to Fe^{2+} at 710.8 and 724.2 eV and Fe^{3+} at 712.9 and 726.8 eV. These fitted components support the presence of mixed-valence Co and Fe species, which may contribute to polaronic charge transport.

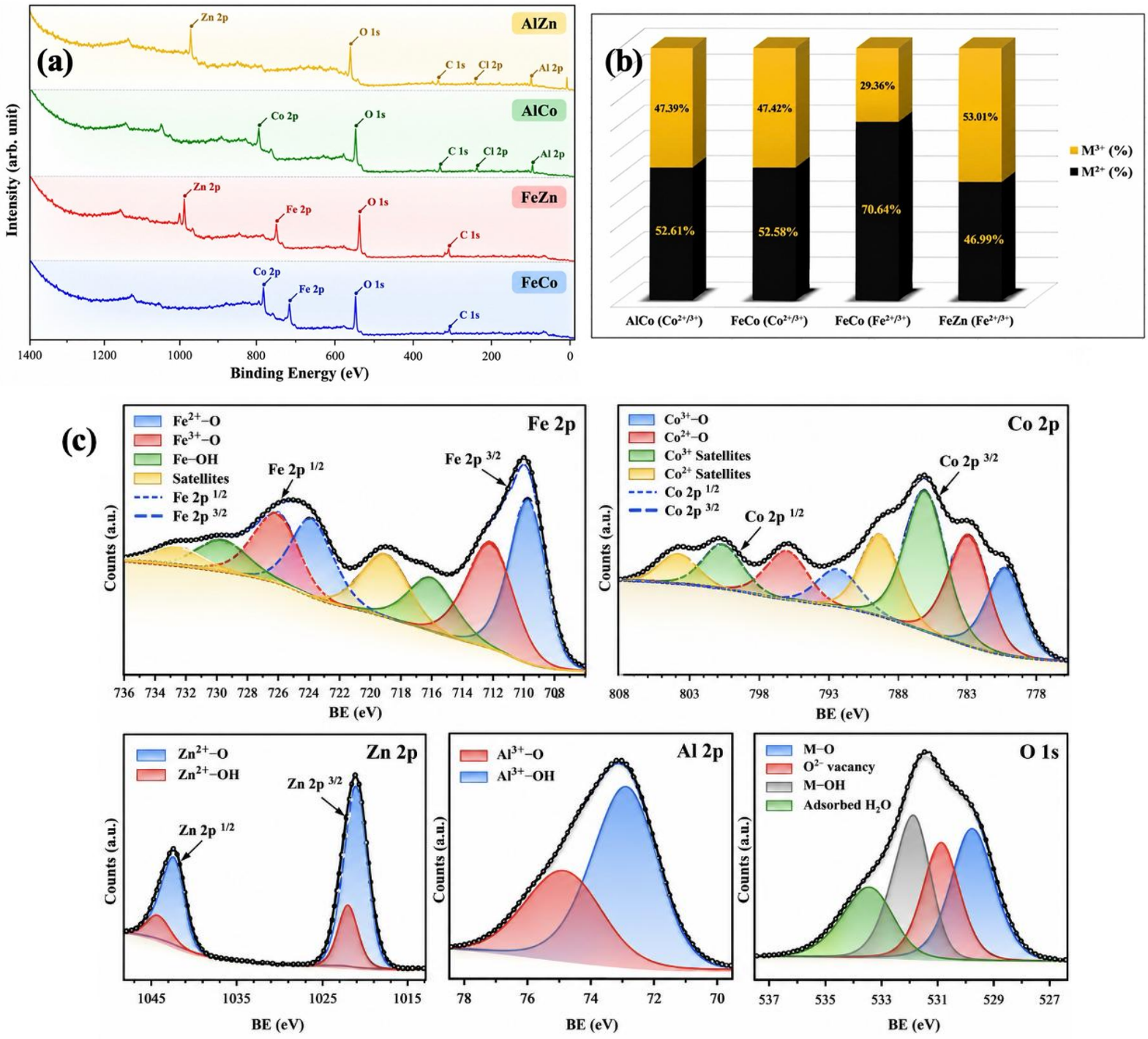

Fig. 4. XPS analysis **(a)** survey spectra. **(b)** Quantitative distribution of metal oxidation states (M^2/M^{3+}). **(c)** high-resolution XPS spectra with peak deconvolution.

3.4. Density and molar volume measurements

Evaluating the density (ρ) and molar volume (V_m) provides fundamental insights into the structural compactness, packing efficiency, and atomic coordination within the LDH host layers[6], [9] .Toluene (ρ = 0.8669 g.cm^{-3}) was selected as the immersion medium due to its chemical inertness toward the LDHs and negligible solubility. Each sample was weighed both in air $W_{t,\,Air}$ and while fully immersed in toluene $W_{t,\,Toluene}$ using a high-precision analytical balance (±0.0001 g). All measurements were performed in three times to ensure reproducibility, with the average values recorded. The obtained values of ρ and V_m are listed in **Table 2**. The experimental density (ρ) was computed via:

$$\boldsymbol{\rho = \rho_{toluene}\left(\frac{Wt,\,Air}{Wt,\,Air - Wt,\,Toluene}\right) \times 0.86\ g.cm^{-3}}\ (9)$$

The corresponding molar volume (V_m) was subsequently calculated from the molecular weight (M_w) and the measured density:

$$\boldsymbol{V_m = \frac{M_w}{\rho}}\ (10)$$

As displayed in **Fig. 5**, exhibits an inverse relationship with V_m, which aligns with classical solid-state theory. The experimental density follows the descending order: FeCo > FeZn > AlCo > AlZn, whereas the molar volume follows the opposing sequence. This systematic variation is mainly governed by the atomic mass and ionic radii of the incorporating trivalent (M^{3+}: Fe^{3+} vs. Al^{3+}) and divalent (M^{2+}: Co^{2+} vs. Zn^{2+}) cations. The considerably higher atomic weight of iron (55.85 g.mol^{-1}) relative to aluminum (26.98 g.mol^{-1}) accounts for the higher density of Fe-Based LDHs over their Al-based counterparts. Also, The lower molar volume of FeCo suggests a more compact structure with closer packing of metal ions and interlayer anions [3] , [4]. To calculate the transition-metal ion concentration per unit volume (N_{TM}) was calculated using:

$$\boldsymbol{N_{TM} = \frac{\rho\, N_A}{M_w}}\ (11)$$

Where $N_A$is Avogadro's number (6.022×10^{23} mol^{-1}). Since the four investigated LDHs have an equimolar metal composition, the concentration of each individual metal ion is given by:

$$\boldsymbol{N_{\frac{Fe}{Al}} = N_{\frac{Co}{Zn}} = \frac{N_{TM}}{2}}\ (12)$$

The slightly higher ion concentration of FeCo is consistent with its higher density and lower molar volume. Furthermore, the mean interionic distance (R_i) between active transition-metal centers was evaluated using the spartial sphere approximation [10] :

$$\boldsymbol{R_i = \left(\frac{1}{N_{Tm}}\right)^{\frac{1}{3}}}\ (13)$$

As listed in **Table 2**, the total transition-metal ion concentration (N_{TM}) in FeCo, yielding the shortest interionic separation and smallest polaron radius. In contrast, as the density declines in FeZn, AlZn, and AlCo, R_i expands up. The shorter interionic distance and smaller polaron radius in FeCo may facilitate charge transfer and hopping conduction.

Sample	ρ ± 0.02 (g.cm^{-3})	M_w (g.mol^{-1})	V_{m} ± 0.02 (cm^3.mol^{-1})	$N_{\mathrm{TM\ ions}}$ ± 0.01 (×10^{22} cm^{-3})	$N_{M^{3+}}$ ± 0.01 (×10^{22} cm^{-3})	$N_{M^{2+}}$ ± 0.01 (×10^{22} cm^{-3})	R_{i} (Å)
FeCo	2.71	39.28	39.28	1.53	7.67	7.67	4.025
FeZn	2.52	42.46	42.46	1.42	7.09	7.09	4.131
AlZn	2.22	42.97	42.97	1.40	7.01	7.01	4.153
AlCo	2.20	43.13	43.13	1.39	6.98	6.98	4.148

Table 2. Physical and polaron-related parameters of the LDH samples.

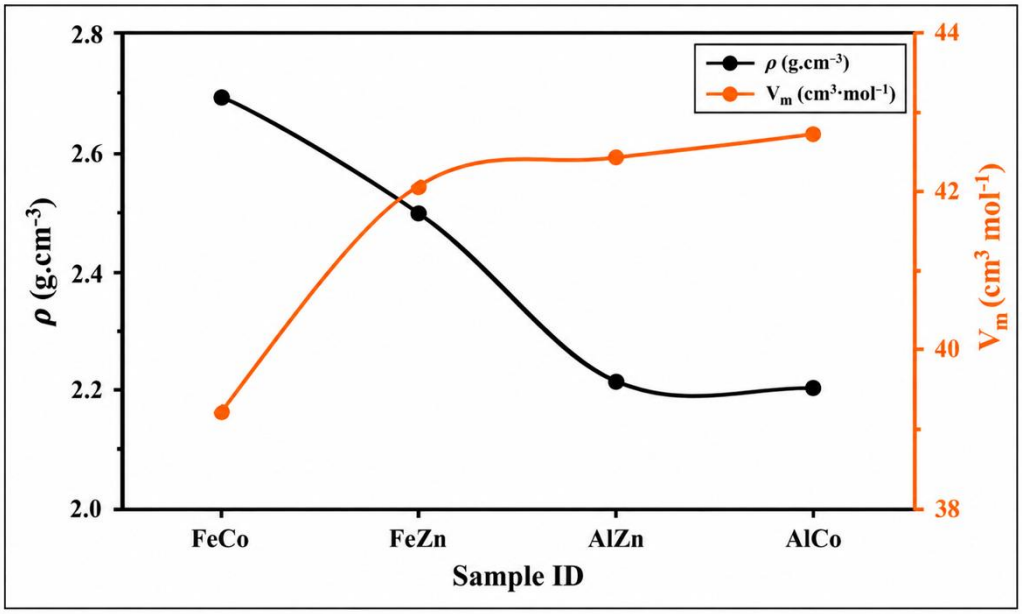

Fig. 2 Density and molar volume changes of LDHs samples

3.4. Thermoelectric power properties (TEP)

Thermoelectric power (TEP) was measured to study the charge-transport behavior of the prepared LDH samples and identify the main charge-carrier type with temperature [6], [11]. In transition-metal oxides and hydroxides, TEP also reflects localized charge transport and small-polaron hopping [6] [12] .The Seebeck coefficient (S) was determined over the 300–420 K regime using a steady-state dual-heater method according to **Eq.14** [13][14]:

$$\boldsymbol{S = \frac{\Delta V}{\Delta T}} \quad \textbf{(14)}$$

Where ΔV the thermoelectric voltage is generated across the sample endpoints and ΔT is the applied temperature difference [13], [14]. A positive S indicates hole-dominated (p-type) transport, whereas a negative S indicates electron-dominated (n-type) conduction [6][15] .The samples exhibit different Seebeck behaviors depending on their cation composition [13][3] : FeCo maintains a negative Seebeck coefficient across the entire temperature range, confirming electron transport via thermally activated hopping between mixed-valence Fe centers [13][16] . FeZn shows a change in sign with temperature, shifting from positive at lower temperatures to negative with heating [13] . This reflects a transition toward dominant electron transport, driven by the change in electronic states when replacing Co with Zn [13][3] . AlCo changes from slightly negative near room temperature to positive upon heating, exhibiting a broad peak [13] . This changing trend suggests contributions from different charge carriers with increasing temperature [6][13] . AlZn exhibits a positive Seebeck coefficient over the entire range [13] , where the steady increase in S reflects thermally activated hole conduction along the hydroxide sheets [13]. To understand localized hopping transport, the Seebeck coefficient was analyzed using the Heikes model [17] :

$$\boldsymbol{S = \frac{k_B}{e} \ln \left(\frac{C}{1 - C}\right)} \quad \textbf{(15)}$$

Where k_B is the Boltzmann constant, e is the elementary charge, and C represents the fraction of reduced transition-metal ions relative to total hopping sites [17]. The fraction (C) is expressed as:

$$\boldsymbol{C = \frac{M^{n+}}{\sum M} = \frac{M^{n+}}{M^{n+} + M^{(n+1)+}}} \quad \textbf{(16)}$$

Where M^{n+} and $M^{(n+1)+}$ represent the concentrations of the lower- and higher-valence metal ions, respectively. Substituting **Eq.15** into **Eq.16** yields the Seebeck coefficient as a function of the valence ratio [8,12]:

$$\boldsymbol{S = \frac{k_B}{e} \ln \left(\frac{M^{n+}}{M^{(n+1)+}}\right)} \quad \textbf{(17)}$$

Within this framework, C = 0.5 represents an equal population of reduced and oxidized states; thus, C < 0.5 corresponds to a negative thermopower, whereas C > 0.5 results in a positive response [17] . The values of C calculated at 400 K are shown in **Fig. 6** and listed in **Table 2** [3] [16]. Importantly, C was not evaluated for AlZn because both exhibit fixed oxidation states, as discussed in the XPS analysis. As presented in **Fig. 6**, the

trend in C directly matches that of: AlCo exhibits the highest C value and most positive Seebeck magnitude, indicating the highest fraction of reduced Co^{2+} sites. FeZn shows the lowest C value, reflecting the lowest fraction of reduced Fe sites. Because electrical conductivity follows ($\sigma = ne\mu$), a larger C increases the number of available hopping sites but does not alone ensure higher conductivity or power factor [16][17]. The transport-derived C values at 400 K were compared with XPS-derived oxidation-state fractions. The comparison showed qualitative agreement between the transport-derived C values and XPS oxidation-state fractions, with slight differences due to the surface sensitivity of XPS (~ 2-5 nm) and the bulk-sensitive nature of TEP [6]. The thermoelectric power factor (PF) was then calculated to evaluate the energy-conversion performance of the LDH samples:

$$\boldsymbol{PF = s^2\sigma} \quad \textbf{(18)}$$

where σ is the electrical conductivity [18] . The temperature dependence of PF (300–420 K) is illustrated in **Figure 7(b)**. Across all compositions, PF increases continuously with temperature, reflecting thermally activated hopping that enhances both carrier mobility and conduction pathways [11]. The comparative PF responses at 323 K and 400 K are presented in **Figure 7(c-d)**. Across both temperature regimes, FeCo maintains the highest power factor, driven by its dense ionic packing, small interionic distance (R_i), and active dual-redox hopping Fe^{2+}/Fe^{3+} and Co^{2+}/Co^{3+} redox channels [16]. In contrast, AlZn displays a strong thermal activation at elevated temperatures, leading to a steeper increase in PF compared to FeZn and AlCo. Meanwhile, the high-temperature decline in AlCo results from an unfavorable balance between its Seebeck coefficient and electrical conductivity [13][18] . Importantly, the highest localized site occupancy (C) in AlCo (★) does not yield the highest PF, while FeZn (▼) shows significant thermal improvement despite its lower initial site occupancy [3]. This demonstrates that the reduced-ion fraction alone does not determine thermoelectric performance, as carrier mobility and electrical conductivity are equally critical [6], [11] . Therefore, the subsequent DC conductivity analysis is required to decouple the individual contributions of mobility and activation energy [6] .

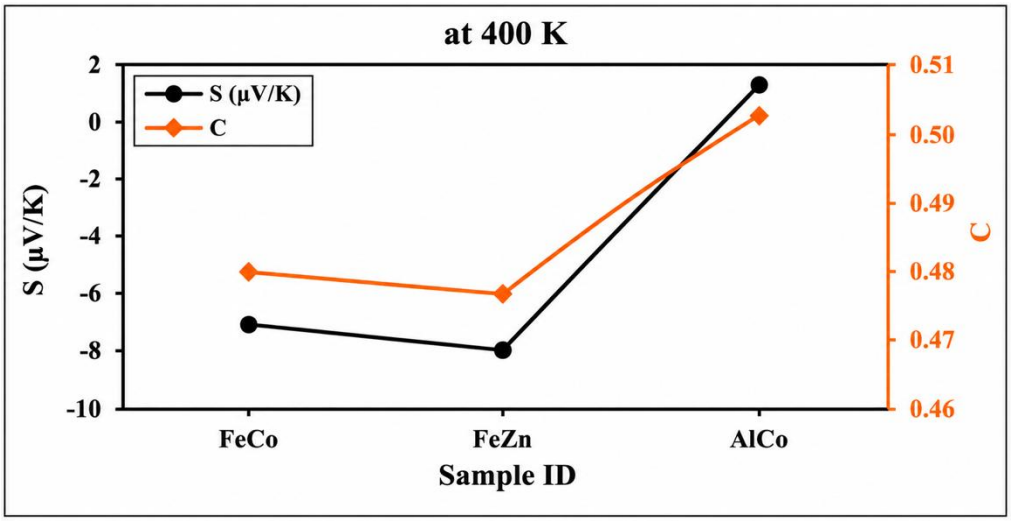

Fig. 6 Thermoelectric Seebeck coefficient (S) and carrier concentration (C) of the LDH samples at 400 K.

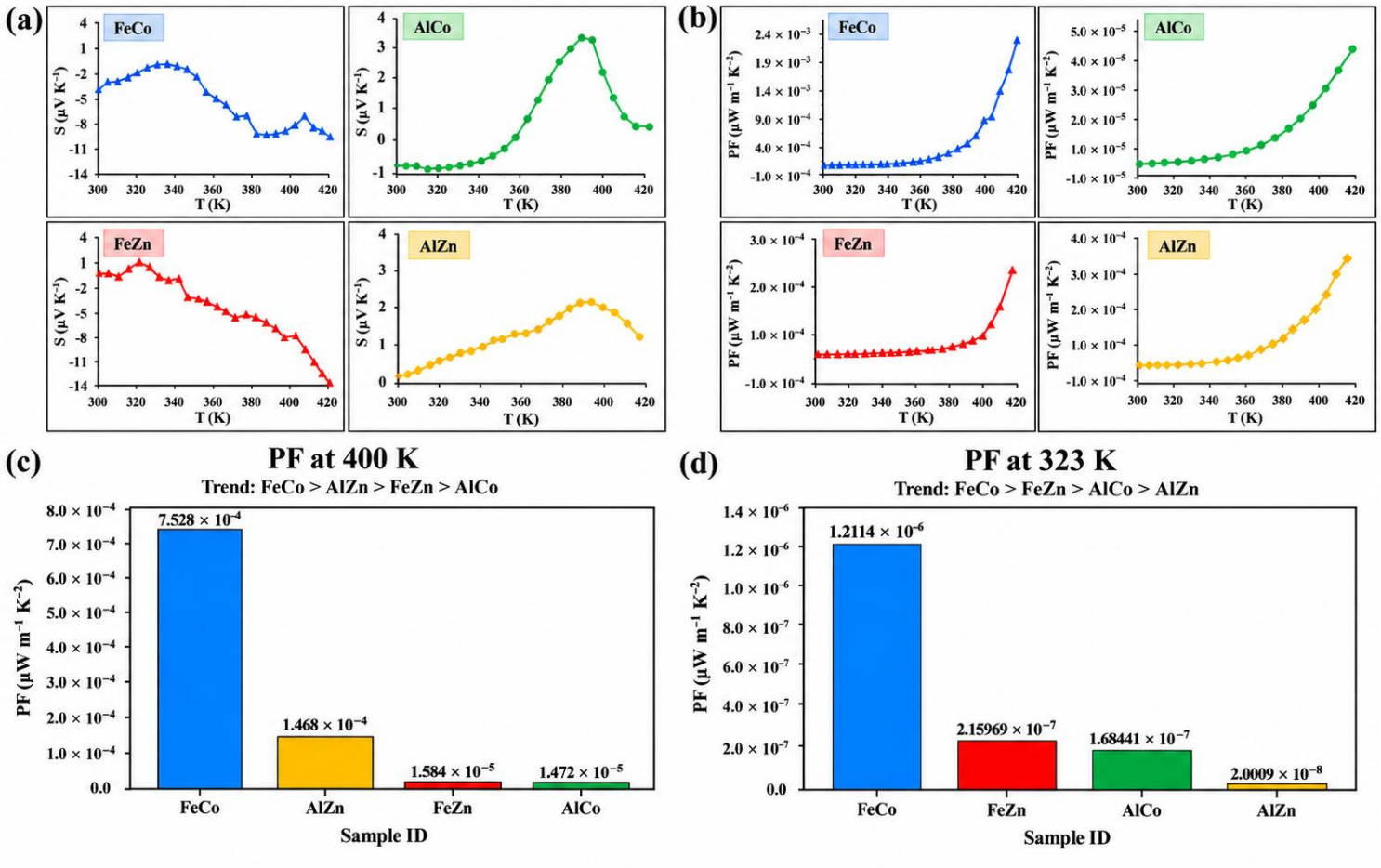

Fig. 7(a) Seebeck coefficient, **(b)** power factor, **(c)** PF at 400 K, and **(d)** PF at 323 K for the LDH samples.

Sample ID	S ± 1 at 400 K ($\mu V \cdot K^{-1}$)	C from TEP	Reduced/Oxidized Ratio (TEP)	C from XPS
FeCo	−7.18	0.4792	0.9201	0.7064 (Fe) / 0.5261 (Co)
FeZn	−8.03	0.4767 [▼]	0.911	0.4699 (Fe)
AlCo	1.28	0.5037 [★]	1.015	0.5258 (Co)
AlZn	1.96	N/A	N/A	N/A

Table. 2 Thermoelectric and XPS-derived electronic parameters of the LDH samples.

3.5. Electrical Conductivity

3.5.1. DC Conductivity and activation energy

The temperature-dependent direct-current (DC) electrical conductivity (σ) was measured from 300 K and 425 K to clarify the charge-transport dynamics in the LDH samples. **Fig. 8(a)** illustrates log σ as a function of (1000/T). Across the tested temperature window, each composition displays two distinct transport regimes separated by a characteristic crossover temperature ($T_{cross} = \theta_D/2$), where θ_D is the Debye temperature [6], [19].Within high-temperature regime ($T > \theta_D$): log σ follows a strictly linear Arrhenius-type response, confirming nearest-neighbor Small Polaron Hopping (SPH) mediated by optical phonons [6] [20]. Low-temperature regime ($T < \theta_D/2$): The curves deviate from linearity, indicating a crossover into Mott's Variable-Range Hopping (VRH) regime as multi-phonon absorption processes freeze out [6] ,[10].

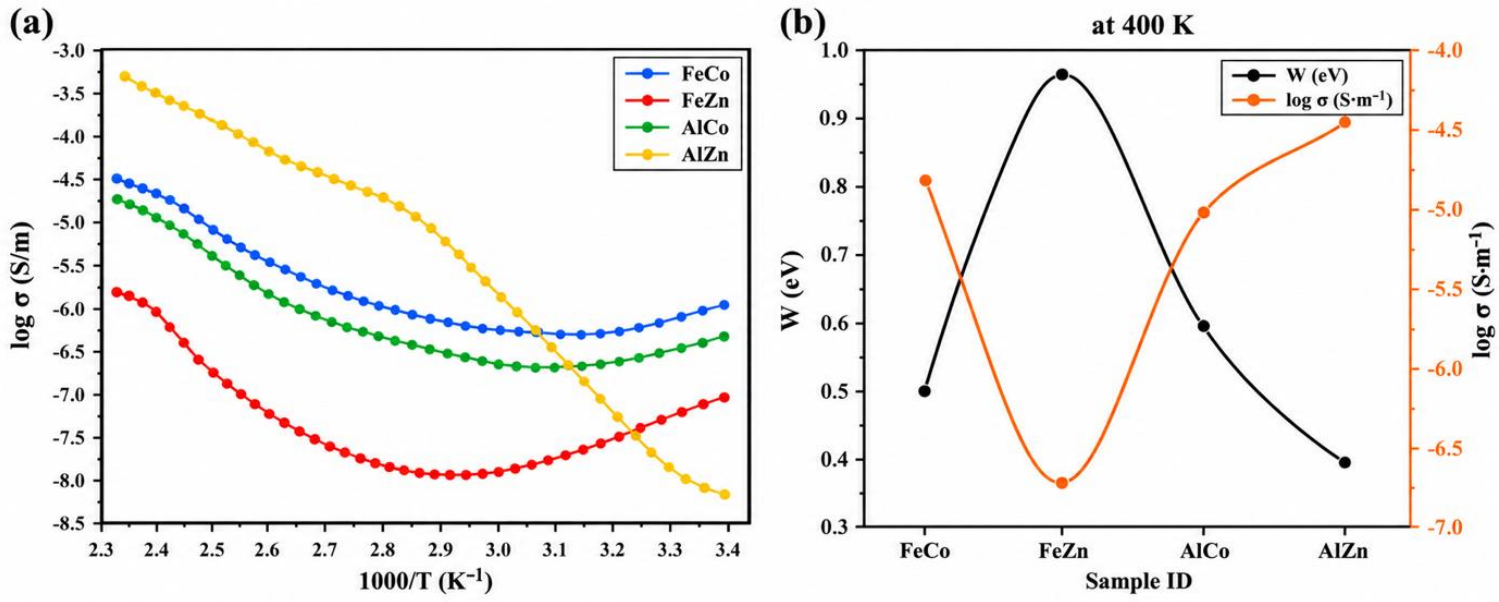

Fig. 3 (a) Arrhenius plots of log σ versus 1000/T; **(b)** hopping energy (W) and conductivity at 400 K.

Sample ID	$\theta_D \pm 1$ (K)	$\nu_0 \pm 0.01$ ($\times 10^{13}$ Hz)	W ± 0.01 (eV)	Log σ ± 0.01 at 400 K (S·m^{-1})
FeCo	666.3	1.388	0.494	-4.813
FeZn	686.3	1.43	0.981	-6.7
AlCo	636.3	1.326	0.598	-5.005
AlZn	626.5	1.305	0.397	-4.373

Table 3. Thermal and electrical transport parameters of the synthesized LDHs

Within the linear high-temperature SPH domain, the electrical conductivity is described by the thermally activated hopping model [6] ,[10]:

$$\boldsymbol{\sigma = \sigma_0 \exp(-\frac{W}{K_B T})} \quad \textbf{(19)}$$

where σ_0 is the pre-exponential factor, K_B is the Boltzmann constant, and W is the thermal activation energy for hopping conduction [6] ,[21] . The activation energy (W) was calculated from the linear slope (m) according to W = -1000 m K_B ln (10). The crossover temperature (T_{cross}) was used to determine the characteristic Debye temperature ($\theta_D = 2\ T_{cross}$) and the optical phonon frequency (ν_o) via **Eq.20** [22], where h is Planck's constant. The evaluated values of Tcross, θ_D, and ν_o are compiled in **Table 3** [23] .

$$\boldsymbol{vo = \frac{K_B \theta_D}{h}} \quad \textbf{(20)}$$

The resulting phonon frequencies are on the order of 10^{13} Hz, matching standard lattice vibration modes in transition-metal hydroxide networks. The relationship of activation energy (W) and DC conductivity (log σ) at 400 is plotted in **Fig. 8(b)** [19][22]. An opposite trend is clear: samples that need higher activation energies show lower electrical conductivities, which is common for thermally activated polaronic transport: FeZn exhibits the highest activation energy (W = 0.981 eV) and the lowest conductivity (log σ = -6.700 S·m^{-1}) [22] . This directly correlates with the TEP findings discussed earlier, where FeZn yielded the lowest localized fractional carrier occupancy (C = 0.4767, marked by ▼). Fewer Fe^{2+} sites may limit electron hopping and increase the energy barrier for charge transfer. FeCo combines a moderate activation energy (0.494 eV) with a high conductivity (-4.813 S·m^{-1}) [22]. This transport efficiency is supported by its dense structural packing, shortest interionic distance (R_i = 4.03 Å), and smallest polaron radius (r_p = 1.62 Å) derived from density measurements, which facilitate electron hopping between adjacent Fe^{2+}/Fe^{3+} and Co^{2+}/Co^{3+} sites. AlCo displays an intermediate activation energy (0.598 eV) and conductivity (-5.005 S·m^{-1}) [22] , consistent with its single active Co^{2+}/Co^{3+} redox channel. For non-adiabatic small polaron hopping, conductivity is quantitatively governed by the Austin–Mott relation:

$$\boldsymbol{\sigma = \frac{\nu_0 N e^2 R^2}{k_B T}\ C(1-C) \exp(-2\alpha R) \exp(-\frac{W}{k_B T})} \quad \textbf{(21)}$$

where N is the metal ion concentration, R is the hopping distance, C is the fraction of hopping sites, and α is the wave-function decay factor. Consequently, the high site occupancies in FeCo and AlCo provide a reliable baseline for polaronic migration. In contrast to the multivalent transition-metal samples, AlZn exhibits the lowest activation energy (W = 0.397 eV, marked by ★) and the highest conductivity at 400 K (log σ = -4.373 $S \cdot m^{-1}$) [22]. Although AlZn shows the lowest conductivity at room temperature, it increases rapidly with temperature. Importantly AlZn LDHs do not display ordinary band conduction because their large bandgap (> 3.5 eV) prevents electron moving across the bandgap at moderate temperatures. Furthermore, because both Al^{3+} ($2p^6$) and Zn^{2+} (d^{10}) possess closed-shell configurations, charge transport cannot occur via localized transition-metal d–d redox hopping. Instead, the unusual electrical behavior of AlZn is driven by two synergistic mechanisms:

1. Grotthuss Proton-Hopping Dynamics: The small ionic radius of Al^{3+} (0.535 Å) provides a high charge-to-radius ratio that strongly affects nearby O–H bonds. Upon thermal excitation, this facilitates rapid proton transfer (H^+) across the continuous interlayer water and hydroxyl network via the Grotthuss mechanism.

2. Thermally Activated Release of Trapped Charge Carriers: At low temperatures, localized carriers are unable to move freely within shallow defect states and grain-boundary potential traps. With heating toward 400 K, these carriers gain enough heat energy to overcome interfacial barriers via thermionic emission, leading to the observed sharp increase in conductivity prior to high-temperature structural dehydration [24] .

3.5.2. Parameters of small polaron hopping

The parameters governing small polaron hopping (SPH) transport was evaluated using the classical Holstein model and Bogomolov formulations [25], [26], compiled in **Table 4**. According to Bogomolov et al. [26] , the localized polaron radius (r_p) correlates directly with the mean intersite distance (R) as:

$$r_p = \frac{R}{2}\left(\frac{\pi}{6}\right)^{1/3} \quad (22)$$

The calculated values of r_p range from 1.62 to 1.67 Å. For all investigated LDH samples, the fundamental spatial criterion for small polaron localization ($r_p < R$) is satisfied ($r_p \approx 0.403\ R$), suggesting that the charge carriers are localized within individual metal centers rather than spread across the crystal lattice [25].

Sample ID	$r_p \pm 0.001$ (Å)	$W_H \pm 0.01$ (eV)	N (E_f) ($\times 10^{21}$ $ev^{-1}cm^{-3}$)	$h\nu_0$ (eV)	γ_p
FeCo	1.622	0.25	7.41	0.0574	4.30
FeZn	1.665	0.49	3.45	0.0591	8.29
AlCo	1.674	0.30	5.58	0.0548	5.45
AlZn	1.672	0.20	8.44	0.0540	3.67

Table 4. Calculated Electronic Transport Parameters

In polar lattices, the polaron hopping activation energy (W_H) can be expressed theoretically via the effective dielectric contribution[25] :

$$\boldsymbol{W_H = \frac{e^2}{4\varepsilon_p}\left(\frac{1}{r_p} - \frac{1}{R}\right)} \quad \textbf{(23)}$$

where ε_p represents the effective dielectric permittivity defined as $(1/\varepsilon_\infty - 1/\varepsilon_s)^{-1}$, while ε_∞ and ε_s being the high-frequency and static dielectric constants, respectively. In three non-adiabatic hopping frameworks formulated by Austin and Mott [6] , the total activation energy (W) obtained from high-temperature Arrhenius plots consists of polaron hopping energy (W_H) and disorder energy (W_D) through $W = W_H + \frac{1}{2}W_D$. For systems dominated by structural hopping barriers, W_H represents the primary energetic barrier opposing charge carrier movement between neighboring cations ($W_H \approx W/2$) [6], [20]. The density of localized states near the Fermi level, $N(E_F)$, was calculated following the Holstein relation [10], [25] :

$$\boldsymbol{N(E_F) = \frac{3}{4\pi R^3 W}} \quad \textbf{(24)}$$

The obtained $N(E_F)$ values fall within the range of 3.45×10^{21} to 8.44×10^{21} $eV^{-1}.cm^{-3}$. These values are consistent with the characteristic localized state densities reported for transition-metal hydroxide matrices and disordered semiconducting oxides [10]. The magnitude of the electron–phonon interaction parameter (γ_p) was evaluated via the relation [25] :

$$\boldsymbol{\gamma_p = \frac{2W_H}{h\nu_0} = \frac{2W_H}{k_B\theta_D}} \quad \textbf{(25)}$$

where ν_0 is the characteristic optical phonon frequency deduced from the Debye temperature (θ_D) through $h\nu_0 = k_B\theta_D$ [10], [25] . According to Mott and Davis, the condition $\gamma_p > 4$ confirms the existence of a strong electron–phonon interaction regime. The evaluated polaronic parameters display clear changes that correlate consistently with the overall DC electrical conductivities across the prepared samples. Specifically, the strongly reduced charge transport observed in FeZn results from strong local lattice distortion and strong electron–phonon coupling, which create deep energy traps prevent trapped carriers from moving and minimize electrical conductivity. In contrast, charge transfer in FeCo is markedly facilitated by reduced hopping barriers across the synergistic Fe^{2+}/Fe^{3+} and Co^{2+}/Co^{3+} redox pathways, whereas carrier migration in AlCo is limited to isolated Co sites dispersed within the electrochemically inert Al^{3+} structure, leading to moderate charge transport. Most remarkably, AlZn exhibits an optimized structural framework characterized by minimal hopping resistance, high localized state density, and the weakest effect of lattice vibrations on electron transport, reflecting lowered lattice strain that promotes fast charge transport and accounts for its superior high-temperature conductivity surge.

3.5.3. The nature of polaron hopping conduction

To understand the charge transport mechanism in the synthesized LDH materials, the nature of the small polaron hopping (SPH) process whether adiabatic or non-adiabatic was comprehensively evaluated using three supporting criteria. In the adiabatic hopping type, the carrier adapts quickly to the lattice vibrations, yielding an electronic transfer probability close to ($P \sim 1$) and an invariant pre-exponential factor (σ_0) across isomorphic compositions [6], [27] . In contrast, non-adiabatic hopping involves a transfer probability much lower than ($P << 1$), making charge transport critically dependent on the spatial overlap integral (J) between adjacent localized states as well as multi-phonon activation dynamics s[6], [27] .

$$\boldsymbol{log_{10}\,\sigma = log_{10}\,\sigma_0 - \frac{W}{2.303\,k_BT}} \quad \textbf{(26)}$$

The primary assessment was conducted by analyzing the linear dependence of the DC conductivity ($\log_{10}\sigma$) on the activation energy (W) at an experimental temperature of T_{exp} = 400 K, as illustrated in **Fig. 9(b)**. The experimental data exhibited an excellent linear correlation (R^2 = 0.9911), yielding a slope of -3.9662 eV^{-1}. According to the Emin-Holstein framework, the calculated temperature (T_{cal}) extracted from the slope was found to be approximately 1270 K. The massive difference between T_{cal} and T_{exp} ($T_{cal} >> T_{exp}$) strongly argues against the adiabatic hopping mechanism and provides strong experimental evidence for non-adiabatic conduction across all four LDH compositions [6], [27] .

$$\boldsymbol{J < RHS = \left(\frac{2W_H\,k_BT}{\pi}\right)^{1/4}\left(\frac{h\nu^0}{\pi}\right)} \quad \textbf{(27)}$$

$$\boldsymbol{J = e^2\left[\frac{N(E_F)}{\left(4\pi\varepsilon_0\varepsilon_p\right)^3}\right]^{1/2}} \quad \textbf{(28)}$$

$$\boldsymbol{J = W_H \exp(-\alpha R)} \quad \textbf{(29)}$$

To support this conclusion at the quantum-mechanical level, the Holstein-Emin bandwidth criterion was evaluated by comparing the polaron bandwidth (J) against the critical non-adiabatic threshold (RHS), as compiled in **Table 5** [27] . The optical phonon energy ($h\nu_o$) ranged between 0.0540 and 0.0591 eV, establishing threshold values (RHS) spanning from 0.0337 eV for AlZn to 0.0442 eV for FeZn. The polaron bandwidths evaluated via both the dielectric density-of-states relation (J = 0.0068 to 0.0169 eV) and the spatial wave function attenuation model (J = 0.0031 to 0.0079 eV) consistently satisfied the condition J < RHS across all samples. Furthermore, the small magnitude of J compared to the hopping energy (W_H = 0.198 to 0.490 eV) and the strong electron-phonon coupling coefficients (γ_p > 7.3) support that the carriers are intensely localized

within the transition-metal coordination polyhedra, thereby confirming a canonical non-adiabatic regime [6], [28] .

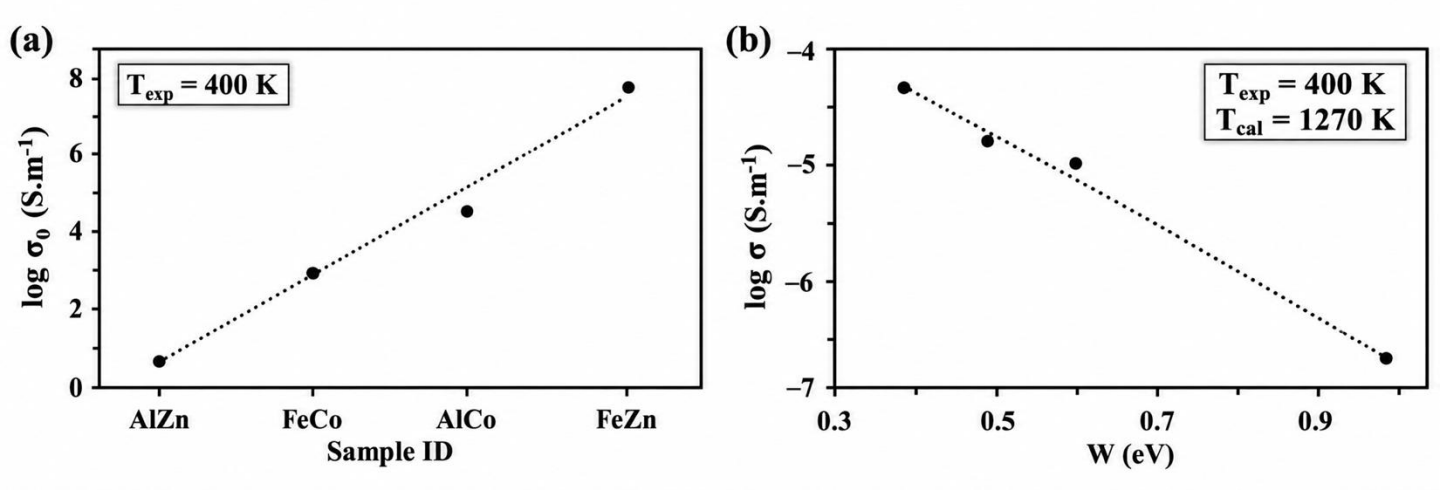

Fig. 9 (a) Meyer–Neldel compensation plot of log σ_0 at 400 K. **(b)** log σ versus activation energy (W), confirming non-adiabatic small-polaron hopping.

Sample ID	J (eV)	RHS at 400 K (eV)	Hopping Regime
AlZn	0.0068	0.0337	Non-Adiabatic
FeCo	0.0085	0.0367	Non-Adiabatic
AlCo	0.0103	0.0376	Non-Adiabatic
FeZn	0.0169	0.0442	Non-Adiabatic

Table 5 Polaron transport parameters

The third definitive evidence emerges from the changes between compositions of the pre-exponential factor (σ_0), depicted in **Fig. 9(a)**. Log_{10} σ_0 increases systematically from 0.53 S.m^{-1} in AlZn to 7.80 S.m^{-1} in FeZn, changing by several orders of magnitude. This large variation argues against the adiabatic expectation of a constant σ_0 and shows the strong dependence on the overlap between neighboring electronic states. The simultaneous increase of σ_0 with increasing activation energy (W) shows the classical Meyer-Neldel compensation rule [29]. In samples with high activation barriers such as FeZn (W = 0.981 eV), polaronic hopping requires cooperative multi-phonon excitations, which naturally increases the activation entropy and increases the pre-factor to compensate for the strong reduction in conductivity due to the energy barrier [29], [30]. In contrast, the lower activation barrier in AlZn (W = 0.397 eV) promotes efficient single-phonon assisted hopping, maintaining superior room- and intermediate-temperature conductivity despite a moderate pre-factor [6] . Consequently, illustrated in **Fig. 9 (b)**, the agreement between the results of T_{cal} >> T_{exp}, J < RHS, and the Meyer-Neldel compensation behavior strongly supports that localized non-adiabatic small polaron hopping is the main electrical conduction mechanism in these layered double hydroxides [6], [27], [29] .

3.5.4. Carrier hopping mobility and density

To determine whether the overall electrical conductivity across the synthesized layered double hydroxides is mainly depends on the concentration of free charge carriers or by their transport efficiency, the hopping carrier mobility (μ) and carrier density (N_c) were determined at a fixed temperature of 400 K. Under the non-adiabatic small polaron hopping regime supported by the Emin-Holstein criteria, the hopping mobility was evaluated using the Austin-Mott formulation [6] :

$$\boldsymbol{\mu = \left(\frac{eR^2}{k_B T}\right)\left(\frac{1}{\hbar}\right)\left(\frac{\pi}{4W_H k_B T}\right)} \quad \textbf{(30)}$$

where e is the elementary charge, R is the average hopping distance, $\hbar$ is the reduced Planck constant, W_H is the polaron hopping energy, J is the electronic transfer integral, and W is the thermal activation energy. The corresponding carrier density was subsequently deduced via the fundamental charge transport relation:

$$\boldsymbol{N_c = \frac{\sigma}{e\mu}} \quad \textbf{(31)}$$

The calculated transport parameters are summarized in **Table 6** and graphically illustrated in **Fig. 10**. Across all four compositions, the hopping mobility remained exceptionally low (μ < 10^{-3} $cm^2.V^{-1}.\ s^{-1}$). Mobilities much lower than the Mott localized threshold of 10^{-2} $cm^2.V^{-1}.\ s^{-1}$ strongly support that the charge carriers do not move through conventional energy bands; instead, they are strongly localized within local environments around transition-metal ions as self-trapped polarons [31] .

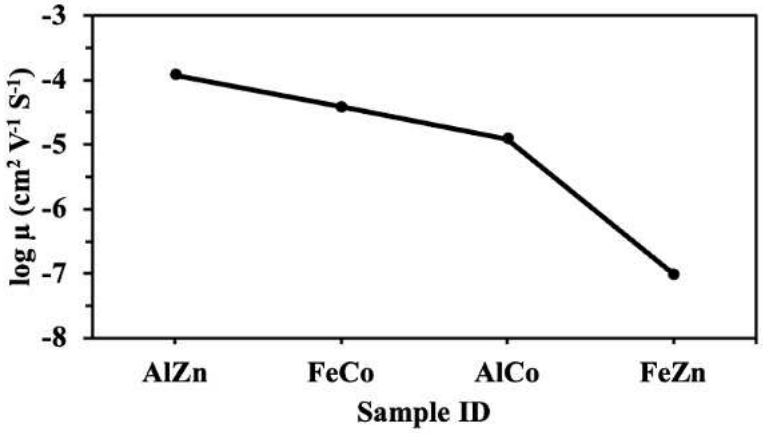

Fig. 10 Variation of hopping carrier mobility (log μ) evaluated at 400 K.

Sample ID	μ ± 0.3 ($cm^2 V^{-1} S^{-1}$)	N_c ± 0.01 (cm^{-3})	A ± 0.1 ($S.m^{-1}K^{1/2}$)	B ± 0.2 ($K^{1/4}$)	α ± 0.01 ($Å^{-1}$)
AlZn	1.19×10^{-4}	2.21×10^{22}	30.39	162.96	2.98
FeCo	3.82×10^{-5}	2.51×10^{22}	37.2	112.75	1.74
AlCo	1.21×10^{-5}	5.12×10^{22}	27.24	156.05	2.45
FeZn	9.7×10^{-8}	1.29×10^{23}	23.96	148.27	1.95

Table 6. Transport and variable-range hopping parameters

Unlike to a very large change modulation observed in mobility, the carrier density (N_c) displayed only a small variation across the samples (2.21×10^{16} to 1.29×10^{17} cm^{-3}). This near-constancy of carrier concentration indicates that the severe reduction in electrical conductivity from AlZn to FeZn is not triggered by a depletion of mobile carriers, but is fundamentally driven by the strong decrease of carrier mobility. The suppressed mobility in FeZn directly correlates with its large hopping energy barrier (W_H = 0.490 eV) and fully occupied $3d^{10}$ electronic shells of Zn^{2+}, which act as strong electrostatic scattering barriers that hinder orbital overlap. In contrast, the AlZn lattice has lower hopping barriers and a high density of states near the Fermi level, allowing polarons to hop with higher velocity and yielding the highest measured mobility [32] .

3.5.5. Intermediate Variable-Range Hopping (VRH) Model

As the temperature decreases below the adiabatic activation zone, multi-phonon cooperative vibrations decrease, and the conduction mechanism changes from hopping between nearby sites to variable-range hopping [33] . In the intermediate-temperature regime, Mott's standard VRH framework is modified according to Greaves' model to include the temperature-dependent density of localized states:

$$\boldsymbol{\sigma T^{1/2} = A \exp\left(-\frac{B}{T^{1/4}}\right)} \quad \textbf{(32)}$$

Linear fitting of log ($\sigma T^{1/2}$) versus $T^{1/4}$ yields the characteristic hopping slope m = -B / 2.303, where the characteristic temperature parameter B is defined by:

$$\boldsymbol{B = 2.1\left[\frac{\alpha^3}{k_B N(E_F)}\right]^{1/4}} \quad \textbf{(33)}$$

Here, α represents the spatial decay parameter of the localized wavefunction, and $N(E_F)$ is the density of states at the Fermi level. The degree of electronic localization is calculated by rearranging this relation:

$$\alpha = \left[\left(\frac{B}{2.1}\right)^4 k_B N(E_F)\right]^{1/3} \quad (34)$$

To evaluate the pre-exponential factor (A) without relying on zero-temperature mathematical estimates that introduce unrealistic values, A was computed using Greaves' microscopic model [34] :

$$A = \frac{e^2}{2} r_p^2 \nu_0 \left[\frac{N(E_F)}{\alpha}\right]^{1/2} \quad (35)$$

where r_p is the polaron radius and ν_0 is the optical phonon frequency extracted from the Holstein criteria. The experimental plots of log ($\sigma T^{1/2}$) against $T^{-1/4}$ demonstrate outstanding linear fitting over the intermediate temperature interval, as displayed in **Fig. 11**. The resulting parameters are compiled in **Table 6**. The modest values of B in FeCo and FeZn reflect lower barriers for charge transfer between sites within mixed-valence transition metal sites. The calculated wavefunction attenuation factor (α) ranged between 1.74 and 2.98 Å^{-1}, corresponding to real-space localization radii (α^{-1}) between 0.34 and 0.57 Å^{-1}. These values are within the typical physical range reported for transition-metal oxide frameworks and confirm strong spatial localization within the metal-oxygen octahedra [35] . Remarkably, AlZn exhibited the highest α value (2.98 Å^{-1}) alongside an elevated B parameter. This reflects the pronounced structural sensitivity of the AlZn lattice: because of its low activation energy (W = 0.397 eV), AlZn transitions rapidly from nearest-neighbor small polaron hopping to variable-range hopping at lower temperatures than Fe- and Co-rich analogues, creating a steeper temperature dependence during the intermediate crossover regime. Furthermore, the calculated pre-exponential factors (A = 23.96 to 37.20 S.m^{-1}. K$^{1/2}$) are within the standard Greaves regime, confirming that intermediate-temperature transport in all four LDH compositions is governed by non-adiabatic variable-range hopping.

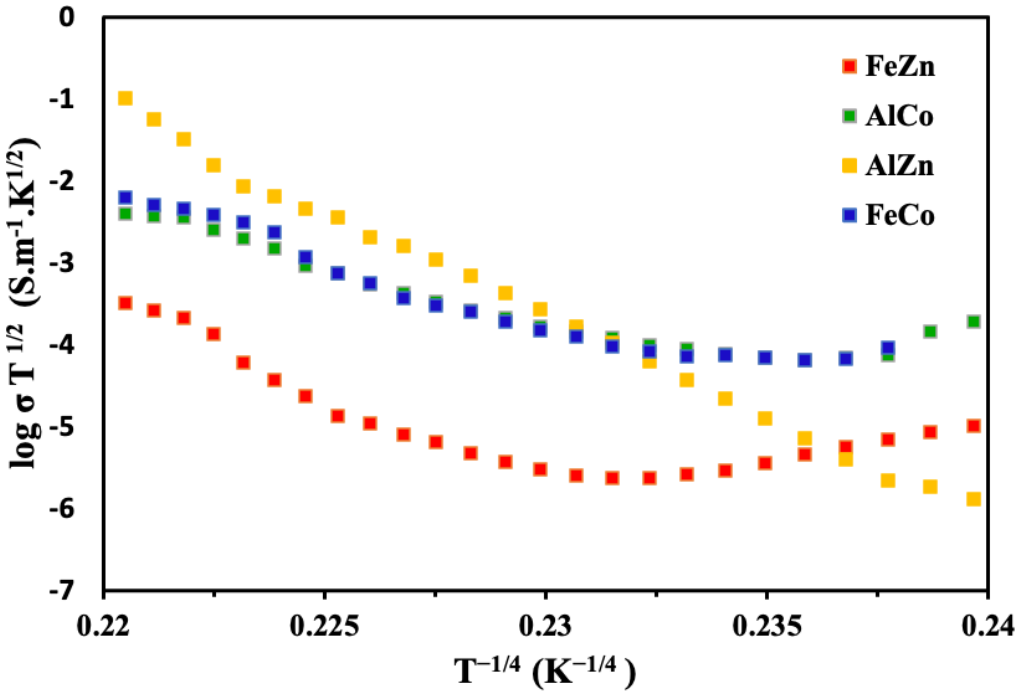

Fig. 11 Plot of log ($\sigma T^{1/2}$) versus $T^{-1/4}$, depicting linear regression fits according to Greaves' intermediate-temperature variable-range hopping (VRH) model.

4. Comparative Electrical Transport in Layered Double Hydroxides

The electrical transport properties of the present equimolar LDHs were compared in **Table.7** with those of the Bi_2O_3-Fe_2O_3-$BaTiO_3$ (BFBT) nanocomposite studied by Gazouly et al.. The authors attributed the conductivity enhancement following heat treatment to non-adiabatic small-polaron hopping between iron centers and reduced grain-boundary scattering. At 400 K, the BFBT sample treated at 1073 K exhibited a DC conductivity of 3.273 x 10^{-5} $S.m^{-1}$ [36]. AlZn-LDH reached 4.236 x 10^{-5} $S.m^{-1}$, approximately 1.29 times this value, whereas FeCo-LDH reached 1.538 x 10^{-5} $S.m^{-1}$. Thus, AlZn-LDH exhibits comparable conductivity without the same high-temperature treatment. Lahkale et al. reported DC conductivities of 6.893 x 10^{-8}, 2.137 x 10^{-7}, and 2.625 x 10^{-7} $S.m^{-1}$ for Mg-Al nitrate LDHs under dry-air conditions at approximately 27% relative humidity [37] . At 400 K, the conductivities of AlZn-LDH and FeCo-LDH were approximately 162 and 59 times higher. Similarly, Kubo and Tadanaga reported a conductivity of 2.7 x 10^{-1} $S.m^{-1}$ for Mg-Al carbonate LDH at 353 K and 80% relative

humidity [38]. These high conductivity values were mainly attributed to hydroxide-ion transport under humid conditions. For NiAl-LDHs, Bouragba et al. reported room-temperature DC conductivities ranging from 3.89 x 10^{-6} to 3.22 x 10^{-5} $S.m^{-1}$, depending on the type of interlayer anion [39]. Maluangnont et al. demonstrated that DC conductivity in NiFe-LDHs depends on layer charge density and temperature. For NF-0.05, the conductivity decreased from approximately 10^{-5} to 10^{-7} $S.m^{-1}$ upon heating, whereas NF-0.25 maintained a value near 10^{-5} $S.m^{-1}$ at elevated temperatures [40]. These contrasting trends were associated with changes in interlayer water and glycerol during heating. The findings indicate that conductivity cannot be explained by metal composition alone; layer charge density and interlayer species also influence charge transport. Ahmed et al. reported conductivities of approximately 10^{-3} to 10^{-2} $S.m^{-1}$ for Zn-Al nitrate LDHs [41] , substantially higher than the 4.236 x 10^{-5} $S.m^{-1}$ measured for AlZn-LDH in the present study. Differences in composition, preparation, and measurement conditions may contribute to this disparity, while humidity-assisted ionic transport may also be relevant to nitrate-containing materials. In a separate study, Ahmed et al. reported conductivities ranging from 6.2 x 10^{-5} to 2.62 x 10^{-4} $S.m^{-1}$ for surfactant-intercalated Zn-Cd-Al dodecyl sulfate LDHs [42] . These values exceed those of the present AlCo-LDH (9.886 x 10^{-6} $S.m^{-1}$) and FeZn-LDH (1.995 x 10^{-7} $S.m^{-1}$) samples, although differences in interlayer structure and measurement conditions limit direct interpretation. Overall, LDH conductivity depends on metal composition, interlayer species, hydration, and measurement conditions. The conductivity and Seebeck results suggest a possible contribution from small-polaron hopping, but further evidence is needed to confirm the transport mechanism and exclude ionic contributions.

Material	Measurement Conditions	DC Conductivity ($S.m^{-1}$)	Ref.
BFBT	400 K; heat-treated	3.27×10^{-5}	[36]
AlMg-NO_3 LDH (Al=20.3%)	Dry air; 27% RH	6.89×10^{-8}	[37]
AlMg-NO_3 LDH (Al=25.4%)	Dry air; 27% RH	2.14×10^{-7}	[37]
AlMg -NO_3 LDH (Al=32.7%)	Dry air; 27% RH	2.63×10^{-7}	[37]
AlMg -CO_3 LDH	353 K; 80% RH	2.70×10^{-1}	[38]
AlNi-LDHs	Room temperature	3.89×10^{-6} to 3.22×10^{-5}	[39]
FeNi-LDH, NF-0.05	298-523 K	1×10^{-5} to 1×10^{-7}	[40]
FeNi-LDH, NF-0.25	298-523 K	1×10^{-5}	[40]
AlZn-NO_3 LDH	Room temperature	1×10^{-3} to 1×10^{-2}	[41]
AlZnCd-SO_4 LDHs	Room temperature	6.2×10^{-5} to 2.62×10^{-4}	[42]
FeCo- CO_3 LDH	400 K; dry vacuum	1.54×10^{-5}	(This work)
AlZn- CO_3 LDH	400 K; dry vacuum	4.24×10^{-5}	(This work)
AlCo- CO_3 LDH	400 K; dry vacuum	9.89×10^{-6}	(This work)
FeZn- CO_3 LDH	400 K; dry vacuum	2.00×10^{-7}	(This work)

Table 7. Comparison of Electrical Conductivity of LDHs and Related Materials

Finally, the structural, electrical, and thermoelectric results collectively indicate that the charge-transport behavior of the four equimolar LDH samples depends on the combined effects of metal composition, local structural order, interionic separation, oxidation states, and carrier mobility. XRD and TEM/SAED suggest that the Al-containing samples exhibit greater structural order, whereas the Fe-containing samples show greater disorder; however, the relationship between crystallinity and conductivity is not straightforward. Although FeCo has the shortest reported mean interionic distance (4.025 Å), which may favor hopping between neighboring sites, AlZn exhibits the highest conductivity at 400 K and the highest calculated hopping mobility ($1.19\text{x}10^{-4}$ $cm^2\ V^{-1}\ s^{-1}$), together with the lowest apparent activation energy (0.397 eV). These findings suggest that transport is governed not only by interionic distance but also by the energy barrier, electronic environment, and mobility of charge carriers. Conversely, FeZn exhibits the highest apparent activation energy (0.981 eV), the lowest calculated mobility ($9.70\text{x}10^{-8}$ $cm^2\ V^{-1}\ s^{-1}$), and the lowest conductivity, consistent with more difficult charge transport in this composition. XPS-derived oxidation-state fractions and thermoelectric-power measurements provide complementary information about possible mixed-valence hopping and carrier behavior: FeCo and FeZn exhibit negative Seebeck coefficients at 400 K, whereas AlCo and AlZn exhibit positive values. The small-polaron hopping and Greaves-type variable-range hopping analyses further suggest that the dominant transport behavior may change with temperature and composition. Nevertheless, the proposed mechanisms

should be interpreted cautiously, because the carrier-density calculations, activation-energy definitions, and some structural parameters require verification. Overall, the results indicate that the balance between hopping mobility, activation barriers, local structure, and electronic states not any single structural parameter—determines the measured transport properties of these LDHs.

Conclusion

This study investigated the structural, electrical, and thermoelectric properties of four equimolar (1:1) layered double hydroxides (LDHs): AlCo, AlZn, FeCo, and FeZn. XRD, TEM/SAED, and XPS analyses revealed composition-dependent differences in structural order and electronic states, with Al-based samples exhibiting greater crystallinity than Fe-based samples. Temperature-dependent conductivity analysis indicated transport behavior consistent with non-adiabatic small-polaron hopping at higher temperatures and Greaves' variable-range hopping at intermediate temperatures. The apparent activation energy ranged from 0.397 eV for AlZn to 0.981 eV for FeZn. At 400 K, AlZn exhibited the highest conductivity and calculated hopping mobility (1.19x 10^{-4} cm^2 V^{-1} s^{-1}), whereas FeZn showed the lowest mobility (9.70 $x10^{-8}$ cm^2 V^{-1} s^{-1}). Thermoelectric measurements also revealed composition-dependent Seebeck responses, including a consistently negative response for FeCo and a positive response for AlZn. Overall, this study establishes a comparative framework for understanding the relationships between metal composition, oxidation states, structural characteristics, and temperature-dependent electronic transport in equimolar LDHs. The combined analysis of electrical conductivity, thermoelectric power, and hopping models provides insight into the factors governing charge transport and may guide the design of LDH-based materials for electronic and thermoelectric applications.

Data Availability Statement: The data supporting the findings of this study are available from the corresponding author upon reasonable request.

Conflict of Interest Statement: The authors declare that they have no known competing financial interests or personal relationships that could have appeared to influence the work reported in this paper.

Funding Statement: This research received no specific grant from any funding agency in the public, commercial, or not-for-profit sectors.

Acknowledgment

The authors would like to express their sincere gratitude to the **Science, Technology & Innovation Funding Authority (STDF), Egypt,** for supporting this research under the **Egyptian–Chinese Cooperation Program,** Project No**. 50375**.

References:

[1] "Polytype Diversity of the Hydrotalcite-Like Minerals I. Possible Polytypes and their Diffraction Features".

[2] A. A. A. Ahmed, Z. A. Talib, and M. Z. bin Hussein, "Thermal, optical and dielectric properties of Zn-Al layered double hydroxide," *Appl. Clay Sci.*, vol. 56, pp. 68–76, Feb. 2012, doi: 10.1016/j.clay.2011.11.024.

[3] F. Cavani, F. Trifirb, and A. Vaccari, "HYDROTALCITE-TYPE ANlONlC CLAYS: PREPARATION, PROPERTIES AND APPLICATIONS."

[4] "Revised effective ionic radii and systematic studies of interatomic distances in halides and chalcogenides", doi: https://doi.org/10.1107/S0567739476001551.

[5] G. K. Williamsont and W. H. Hallt, "X-RAY LINE BROADENING FROM FILED ALUMINIUM AND WOLFRAM*."

[6] I. G. Austin and N. F. Mott, "Polarons in crystalline and non-crystalline materials," *Adv. Phys.*, vol. 18, no. 71, pp. 41–102, Jan. 1969, doi: 10.1080/00018736900101267.

[7] M. A. Ghaleb, R. M. El-Sherif, K. F. Qasim, and M. M. El-Desoky, "Synergistic structural contribution of Co and V doping in nanostructured MoS_2 on its electrochemical performance as a supercapacitor electrode," *J. Energy Storage*, vol. 140, Dec. 2025, doi: 10.1016/j.est.2025.119022.

[8] N. F. Mott, "CONDUCTION IN GLASSES CONTAINING TRANSITION METAL IONS," t~ Nort h-Holland Publishing Co, 1968.

[9] S. E. Zaki *et al.*, "Tin diselenide/zirconium disulfide terahertz acoustic multi-layer superlattice for liquid sensing applications of acetonitrile; reconsidering Voigt-Reuss-Hill schemes," *Results Phys.*, vol. 42, Nov. 2022, doi: 10.1016/j.rinp.2022.106041.

[10] H. A. Alshammari, A. H. Korna, S. S. Fares, B. A. Alshahrani, and N. A. Alshammar, "Impact of $Er^{3+}Ce^{4+}$ Co-doping on the radiation stability and photoluminescence of borotellurite glass-ceramics," *J. Alloys Compd.*, vol. 1077, Jul. 2026, doi: 10.1016/j.jallcom.2026.189374.

[11] "Complex thermoelectric materials", doi: https://doi.org/10.1002/9783527667703.ch10.

[12] "Metal-Insulator Transitions", doi: https://doi.org/10.1201/b12795.

[13] S. E. Zaki *et al.*, "Tin diselenide/zirconium disulfide terahertz acoustic multi-layer superlattice for liquid sensing applications of acetonitrile; reconsidering Voigt-Reuss-Hill schemes," *Results Phys.*, vol. 42, Nov. 2022, doi: 10.1016/j.rinp.2022.106041.

[14] H. J. Goldsmid, "Springer Series in Materials Science 121 Introduction to Thermoelectricity." [Online]. Available: http://www.springer.com/series/856

[15] D. M. Rowe, Ed., *Thermoelectrics Handbook*. CRC Press, 2018. doi: 10.1201/9781420038903.

[16] J. B. Goodenough, "4 METALLIC OXIDES."

[17] "Thermopower in cobalt oxides", doi: https://doi.org/10.1103/PhysRevB.62.6869.

[18] "Perspectives on thermoelectrics: from fundamentals to device applications", doi: https://doi.org/10.1039/c1ee02497c.

[19] S. E. Zaki *et al.*, "Tin diselenide/zirconium disulfide terahertz acoustic multi-layer superlattice for liquid sensing applications of acetonitrile; reconsidering Voigt-Reuss-Hill schemes," *Results Phys.*, vol. 42, Nov. 2022, doi: 10.1016/j.rinp.2022.106041.
[20] A. Yasmin *et al.*, "A first report on ex-situ synthesis and utilization of pure La_4NiLiO_8 in emerging high-performance safe batteries," *J. Alloys Compd.*, vol. 821, Apr. 2020, doi: 10.1016/j.jallcom.2019.153208.
[21] J. B. Goodenough, "4 METALLIC OXIDES."
[22] N. Benreguia, A. Abdi, O. Mahroua, and M. Trari, "Photoelectrochemical properties of the crednerite $CuMnO_2$ and its application to hydrogen production and Mn^+ reduction ($Mn^+ = Cd^{2+}$, Pd^{2+}, Zn^{2+}, Ni^{2+}, and Ag^+)," *Journal of Materials Science: Materials in Electronics*, vol. 32, no. 8, pp. 10498–10509, Apr. 2021, doi: 10.1007/s10854-021-05705-z.
[23] "Perspectives on thermoelectrics: from fundamentals to device applications".
[24] T. Ungár, "Microstructural parameters from X-ray diffraction peak broadening," *Scr. Mater.*, vol. 51, no. 8 SPEC. ISS., pp. 777–781, 2004, doi: 10.1016/j.scriptamat.2004.05.007.
[25] J. Devreese and S. Alexandrov, "Froehlich Polaron and Bipolaron: Recent Developments," Apr. 2009, doi: 10.1088/0034-4885/72/6/066501.
[26] P. Matterhorn, "On Bogoliubov's Kinetic Equation for a Spatially Homogeneous Plasma ANDREW LENARI)."
[27] D. Emin and T. Holstein, "Studies of Small-Polaron Motion IV. Adiabatic Theory of the Hall Effect - EMIN AND HOLSTEIN."
[28] L. Murawski and R. J. Barczyfiski, "Dielectric properties of transition metal oxide glasses," 1995.
[29] "Origin and consequences of the compensation (Meyer-Neldel) law".
[30] "Effect of growth temperature on the structure and magnetic properties of sputtered biepitaxial (111) permalloy films".
[31] N. K. Wally, E. Sheha, H. F. M. Mohamed, I. Morad, K. F. Qasim, and M. M. El-Desoky, "Impact of heat treatment on the structural, positron annihilation parameters, electrical, and electrochemical properties of tin oxide/tin pyrophosphate nanocomposites," *J. Alloys Compd.*, vol. 1040, Sep. 2025, doi: 10.1016/j.jallcom.2025.183399.
[32] N. A. Gazouly, A. E. Hannora, H. A. Yousef, A. M. Ali, and M. M. El-Desoky, "Study of nanostructural and non-adiabatic small polaron hopping conduction in nanostructured Bi_2O_3 - Fe_2O_3 – $BaTiO_3$," *Mater. Sci. Semicond. Process.*, vol. 162, Aug. 2023, doi: 10.1016/j.mssp.2023.107532.
[33] "Conduction in non-crystalline materials".
[34] G. N. Greaves, "SMALL POLARON CONDUCTION IN V2Os-P20 s GLASSES."
[35] R. Orbach, "North-HollandJ°urnal of Non-Crystalline Solids 164-166 (1993) 917-922 ~U: Section 17. Phonons," 1993.
[36] N. A. Gazouly, A. E. Hannora, H. A. Yousef, A. M. Ali, and M. M. El-Desoky, "Study of nanostructural and non-adiabatic small polaron hopping conduction in nanostructured Bi_2O_3 - Fe_2O_3 – $BaTiO_3$," *Mater. Sci. Semicond. Process.*, vol. 162, Aug. 2023, doi: 10.1016/j.mssp.2023.107532.

[37] R. Lahkale *et al.*, "Nitrate-intercalated Mg1−xAlx-Layered Double Hydroxides with different layer charges (x): Preparation, characterization, and study by impedance spectroscopy," *Appl. Clay Sci.*, vol. 158, pp. 55–64, Jun. 2018, doi: 10.1016/j.clay.2018.03.005.

[38] D. Kubo, K. Tadanaga, A. Hayashi, and M. Tatsumisago, "Hydroxide ion conduction mechanism in Mg-Al Co_3^{2-} layered double hydroxide," *Journal of Electrochemical Science and Technology*, vol. 12, no. 2, pp. 230–236, 2021, doi: 10.33961/JECST.2020.01424.

[39] F. Z. Bouragba, W. Elhatimi, R. Lahkale, E. M. Moujahid, and E. Sabbar, "Effect of intercalated anions on the electrical and dielectric properties of NiAl-X layered double hydroxide (X=CO_3^{2-} , NO_3^- and $H_2PO_4^-$): investigation by impedance spectroscopy," *Bulletin of Materials Science*, vol. 43, no. 1, Dec. 2020, doi: 10.1007/s12034-020-2051-6.

[40] T. Maluangnont, S. Sriphan, K. Chaithaweep, N. Vittayakorn, R. P. Wijitwongwan, and M. Ogawa, "AC Electrical Properties of a NiFe-Layered Double Hydroxide with an Exceptionally Low Charge Density," *Journal of Physical Chemistry C*, vol. 129, no. 18, pp. 8756–8763, May 2025, doi: 10.1021/acs.jpcc.5c00982.

[41] A. A. Ali Ahmed, Z. A. Talib, M. Z. Hussein, and Y. A. Ahmed Al-Magdashi, "New DC conductivity spectra of Zn-Al layered double hydroxide (Zn-Al-NO_3-LDH) and its calcined product of ZnO phase," *AIMS Mater. Sci.*, vol. 4, no. 3, pp. 670–679, 2017, doi: 10.3934/matersci.2017.3.670.

[42] A. A. A. Ahmed, Z. A. Talib, and M. Z. Hussein, "Influence of sodium dodecyl sulfate concentration on the photocatalytic activity and dielectric properties of intercalated sodium dodecyl sulfate into Zn-Cd-Al layered double hydroxide," *Mater. Res. Bull.*, vol. 62, pp. 122–131, 2015, doi: 10.1016/j.materresbull.2014.11.026.